Title

Observation of a prethermal discrete time crystal

Journal

Science, 372(6547)

ISSN

0036-8075

Authors

Kyprianidis, A
Machado, F
Morong, W
et al.

Publication Date

2021-06-11

DOI

10.1126/science.abg8102

Peer reviewed

Observation of a prethermal discrete time crystal

A. Kyprianidis[*1†], F. Machado[*2,3], W. Morong[1], P. Becker[1], K. S. Collins[1], D. V. Else[4], L. Feng[1], P. W. Hess[5], C. Nayak[6,7], G. Pagano[8], N. Y. Yao[2,3], and C. Monroe[1]

[1]Joint Quantum Institute, Dept. of Physics and Joint Center for Quantum Information and Computer Science, University of Maryland, College Park, MD 20742 USA

[2]Dept. of Physics, University of California, Berkeley, CA 94720 USA

[3]Materials Sciences Division, Lawrence Berkeley National Laboratory, Berkeley, CA 94720, USA

[4]Dept. of Physics, Massachusetts Institute of Technology, Cambridge, MA 02139 USA

[5]Dept. of Physics, Middlebury College, Middlebury, VT 05753 USA

[6]Microsoft Quantum, Station Q, Santa Barbara, CA 93106 USA

[7]Dept. of Physics, University of California, Santa Barbara, CA 93106 USA

[8]Dept. of Physics and Astronomy, Rice University, Houston, TX 77005 USA

[†]To whom correspondence should be addressed; E-mail: akyprian@umd.edu.

Extending the framework of statistical physics to the non-equilibrium setting has led to the discovery of novel phases of matter, often catalyzed by periodic driving. However, preventing the runaway heating associated with driving a strongly interacting quantum system remains a challenge in the investigation of these new phases. In this work, we utilize a trapped-ion quantum simulator to observe signatures of a non-equilibrium driven phase without disorder: the prethermal discrete time crystal. Here, the heating problem is circumvented not by disorder-induced many-body localization, but rather high-frequency driving, leading to an expansive time window where non-equilibrium phases

[*]These authors contributed equally to the preparation of this manuscript.

can emerge. Floquet prethermalization is thus presented as a general strategy for creating, stabilizing, and studying intrinsically out-of-equilibrium phases of matter.

The periodic modulation of a system represents a versatile technique for controlling its behavior, enabling the emergence of phenomena ranging from parametric synchronization to dynamic stabilization (*1*). Periodic driving has become a staple in fields ranging from nuclear magnetic resonance spectroscopy to quantum information processing (*2–4*). On a more fundamental level, the periodic Floquet drive also imbues a system with a discrete time-translational symmetry. Remarkably, this symmetry can be utilized to protect novel Floquet topological phases, or spontaneously broken to form time-crystalline order (*5–15*).

The realization of many-body Floquet phases of matter requires overcoming two crucial challenges. First, the system must not absorb energy from the driving field. In the presence of a periodic drive, dynamics are not constrained by energy conservation, and Floquet heating causes a generic many-body system to approach infinite temperature, precluding the existence of any non-trivial order (*16*). Second, genuine late-time dynamics must be clearly differentiated from early-time transient behavior: a phase of matter can only be characterized after dynamical processes lead to the steady state behavior.

The conventional strategy for addressing the first (heating) challenge is to utilize strong disorder to induce many-body localization (MBL), where the presence of an extensive set of conserved local quantities prevents Floquet heating (*17*). However, requiring many-body localization leads to its own set of challenges, including stringent constraints on both the dimensionality and the range of interactions (*18, 19*). Moreover, the presence of strong disorder further slows down equilibration, making it even more difficult to overcome the second (timescale) challenge and distinguish between early- and late-time dynamics. Interestingly, long-lived subharmonic responses, characteristic of time-crystalline order, have also been observed in certain

superfluid quantum gases without disorder (*13, 20–22*); the absence of Floquet heating in such systems owes to an effective few-body description of the quantum dynamics (*23*).

Recently, an alternate, disorder-free framework for addressing both these challenges has emerged: Floquet prethermalization (*25–29*). For sufficiently high Floquet drive frequencies, energy absorption by the many-body system requires multiple correlated local rearrangements, strongly suppressing the heating rate. The Floquet heating time τ^* scales exponentially with the drive frequency and can thus be prolonged beyond experimentally practical timescales. For time $t < \tau^*$, the system dynamics are captured by an effective prethermal Hamiltonian $H_{\rm eff}$ (*25, 26*). This prethermal Hamiltonian defines an effective energy for the Floquet system and also determines the nature of the prethermal state, which is reached at the much shorter local equilibration time $\tau_{\rm pre}$. Thus, by focusing on times between $\tau_{\rm pre}$ and τ^*, the dynamics are guaranteed to reflect the actual thermodynamic properties of the Floquet phase.

This intermediate prethermal regime need not be trivial: new symmetries, protected by the discrete time translation symmetry of the drive, can emerge and lead to intrinsically non-equilibrium phases of matter (*30, 31*). One example of such a phase is the prethermal discrete time crystal (PDTC), in which the many-body system spontaneously breaks the discrete time translation symmetry of the drive and develops a robust sub-harmonic response.

A disorder-free PDTC exhibits a number of key differences compared to the MBL discrete time crystal, despite the similarity of their sub-harmonic response (*23, 32*). When stabilized by MBL, time-crystalline order is independent of the initial state and persists to arbitrarily late times, but is believed to only occur in low dimensions with sufficiently short-range interactions (*18, 19*). By contrast, the PDTC lifetime is limited by τ^* and depends on the energy density of the initial state; this energy density determines the prethermal state to which the system equilibrates for times $t > \tau_{\rm pre}$. Crucially, if the prethermal state spontaneously breaks the emergent symmetry of $H_{\rm eff}$, the many-body system also exhibits robust time-crystalline or-

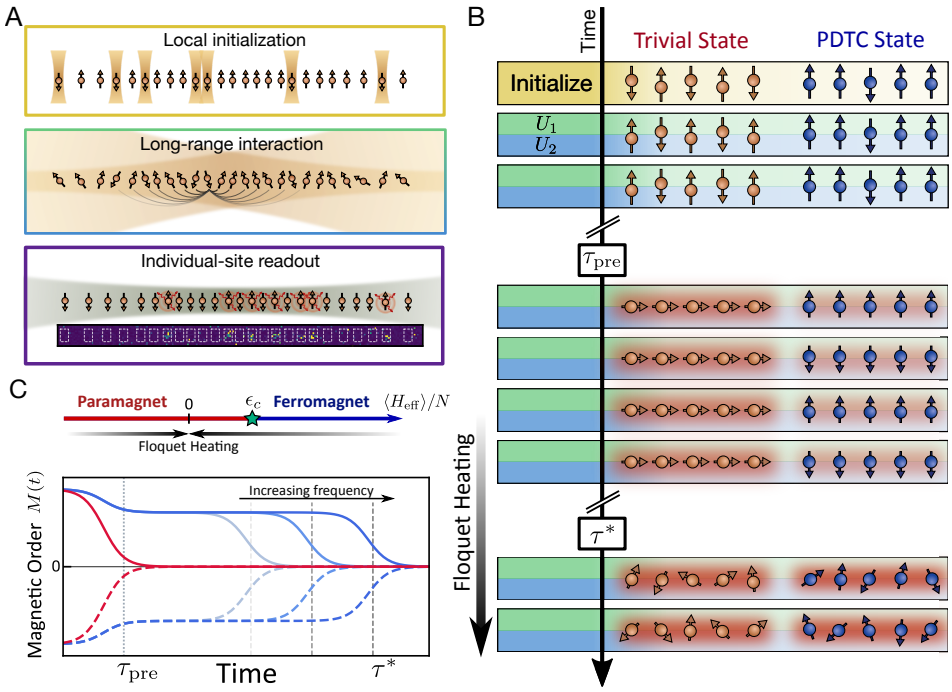

Figure 1: **Experimental setup and protocol**. **A.** Schematic of the 25-ion chain (*24*). Single-site addressing (top), global Raman beams (middle), and state-dependent fluorescence (bottom) enable the preparation, evolution, and detection of the quantum dynamics. **B.** For intermediate times ($\tau_{\rm pre} < t < \tau^*$), the system approaches an equilibrium state of the prethermal Hamiltonian $H_{\rm eff}$. In the trivial Floquet phase, the magnetization after $\tau_{\rm pre}$ decays to zero. In the PDTC phase, the magnetization changes sign every period leading to a robust sub-harmonic response. At times $t \gg \tau^*$, Floquet heating brings the many-body system to a featureless infinite temperature ensemble. **C.** Top: Phase diagram of $H_{\rm eff}$. Owing to the anti-ferromagnetic nature of the Ising interactions $J_{ij} > 0$, the ferromagnetic phase occurs at the top of the many-body spectrum. Bottom: Schematic of the stroboscopic magnetization dynamics in the trivial [red] and PDTC [blue] phase (full/dashed curves represent even/odd driving periods). When the energy density of the initial state is above the critical value $\epsilon_{\rm c}$, the system is in the PDTC phase and its lifetime follows the frequency-dependent heating time τ^*.

der, corresponding to an oscillation between the different symmetry sectors (*30, 31*). On the other hand, if the prethermal state is symmetry-unbroken, the system will be in a trivial Floquet phase, with any signatures of time-crystalline order decaying by $\tau_{\rm pre}$. The requirement of a symmetry-broken phase further distinguishes the PDTC and its MBL counterpart, and highlights the PDTC's stability in higher dimensions. Indeed, in one dimension, Landau-Peierls arguments rule out the existence of a PDTC with short-range interactions (*33*), and long-range interactions are necessary to stabilize a prethermal time crystal (*31*).

We exploit the controlled long-range spin-spin interactions of an ion trap quantum simulator to observe signatures of a one-dimensional prethermal discrete time crystal. Our main results are three-fold. First, we prepare a variety of locally inhomogeneous initial states via individual addressing of ions within the one-dimensional chain (Fig. 1A). By characterizing the quench dynamics starting from these states, we directly observe the approach to the prethermal state, enabling the experimental extraction of the prethermal equilibration time, $\tau_{\rm pre}$. Second, we measure the time dynamics of the energy density as a function of the driving frequency. By preparing states near both the bottom and the top of the spectrum (Fig. 1B), we observe either the gain or loss of energy as the system heats to infinite temperature (corresponding to zero energy density). Importantly, we find that the heating timescale, τ^*, increases with the driving frequency (Fig. 2). Finally, to probe the nature of prethermal time-crystalline order, we study the Floquet dynamics of different initial states that equilibrate to either a symmetry-broken or a symmetry-unbroken ensemble. The former exhibits robust period-doubling behavior up until the frequency-controlled heating timescale, τ^* (Fig. 3B). In comparison, for the latter, all signatures of period doubling disappear by the frequency-independent timescale $\tau_{\rm pre}$ (Fig. 3A). By investigating the lifetime of the time-crystalline order as a function of the energy density of the initial state, we identify the phase boundary for the PDTC.

Our system consists of a one-dimensional chain of 25 $^{171}\mathrm{Yb}^{+}$ ions. Each ion encodes an

effective spin-1/2 degree of freedom in its hyperfine levels $|F=0, m_F=0\rangle$ and $|F=1, m_F=0\rangle$ (Fig. 1A). Long-range Ising interactions are generated via a pair of Raman laser beams (*34, 35*). Arbitrary effective magnetic fields can be applied either locally or globally and single-site readout can be performed simultaneously across the full chain (*24*), enabling the direct measurement of the Floquet dynamics of both the magnetization and the energy density.

The Floquet drive alternates between two types of Hamiltonian dynamics (Fig. 1B): (i) a global π-pulse around the $\hat{y}$ axis and (ii) evolution for time T under a disorder-free, long-range, mixed-field Ising model. This is described by the two evolution operators,

$$\begin{aligned} U_1 &= \exp\left[-i\frac{\pi}{2}\sum_i^N \sigma_i^y\right] \\ U_2 &= \exp\left[-iT\left(\sum_{i<j}^N J_{ij}\sigma_i^x\sigma_j^x + B_y\sum_{i=1}^N \sigma_i^y + B_z\sum_{i=1}^N \sigma_i^z\right)\right], \end{aligned} \tag{1}$$

where σ_i^v is the v-th component of the spin-1/2 Pauli operator for the i-th ion, and we adopt the convention $\hbar = 1$. Here, $J_{ij} > 0$ is the long-range coupling with average nearest-neighbor interaction strength $J_0 = 2\pi \cdot 0.33$ kHz, while $B_y = 2\pi \cdot 0.5$ kHz and $B_z = 2\pi \cdot 0.2$ kHz are global effective magnetic fields. The Floquet unitary $U_F = U_2U_1$ implements the dynamics over a period of the drive and has frequency $\omega = 2\pi/T$.

Within the prethermal window in time $\tau_{\rm pre} < t < \tau^*$, the stroboscopic dynamics of the system (every other period) are well-approximated by an effective prethermal Hamiltonian, which to lowest order in $1/\omega$ is given by (*31*):

$$H_{\rm eff} = \sum_{i<j}^N J_{ij}\sigma_i^x\sigma_j^x + B_y\sum_{i=1}^N \sigma_i^y. \tag{2}$$

A crucial feature of $H_{\rm eff}$ is that long-range Ising interactions stabilize a ferromagnetic phase along the $\hat{x}$ axis. However, owing to the anti-ferromangetic nature of the interactions ($J_{ij} > 0$), this phase does not occur at low energy density close to the bottom of the spectrum, but rather at high energy density near the top of the spectrum (Fig. 1C).

We begin by characterizing the dynamics of the system as it approaches the prethermal state of $H_{\rm eff}$. In particular, we prepare an initial state with all spins pointing along $\hat{x}$ (in an eigenstate of σ^x), except for two central spins, which are prepared along $\hat{z}$ (Fig. 2D). Quench dynamics from this initial state show that the magnetization of the two central spins exhibits two-step dynamics. The $\hat{x}$-magnetization, starting at zero, first equilibrates to the value of the neighboring spins, before decaying back to zero at late times. The convergence of the initially inhomogeneous $\hat{x}$-magnetization to a uniform finite value demonstrates that the system first reaches an intermediate-time equilibrium (i.e. prethermal) state before ultimately heating to infinite temperature. We find that this prethermal timescale is approximately given by $J_0\tau_{\rm pre} \approx 3$.

In addition to $\tau_{\rm pre}$, the prethermal regime is also characterized by the timescale associated with the frequency-dependent Floquet heating, τ^*. To experimentally investigate τ^*, we measure the dynamics of the prethermal energy density, $\langle H_{\rm eff}\rangle/(NJ_0)$, for two different initial states on opposite ends of the many-body spectrum of $H_{\rm eff}$: a low-energy Néel state (Fig. 2A) and a high-energy polarized state (Fig. 2B). In both cases, we observe the expected trend: increasing the driving frequency suppresses the heating rate (Fig. 2C). However, the finite decoherence time of the system (induced by external noise sources) sets an upper bound on the maximum heating time scale; as a result, at large drive frequency, τ^* cannot grow exponentially with increasing drive frequency, but rather approaches a plateau value (*35*). Crucially, even in the presence of this decoherence dynamics, the separation between τ^* and $\tau_{\rm pre}$ enables experimental access to the prethermal regime.

The demonstration of the frequency dependence of τ^* (Fig. 2) directly translates into our ability to control the lifetime of the prethermal time crystal. As aforementioned, the key ingredient underlying time-crystalline order is the presence of an emergent symmetry, G, in $H_{\rm eff}$, which is not a microscopic symmetry present in the Hamiltonian (Eq. 1), but rather, a direct

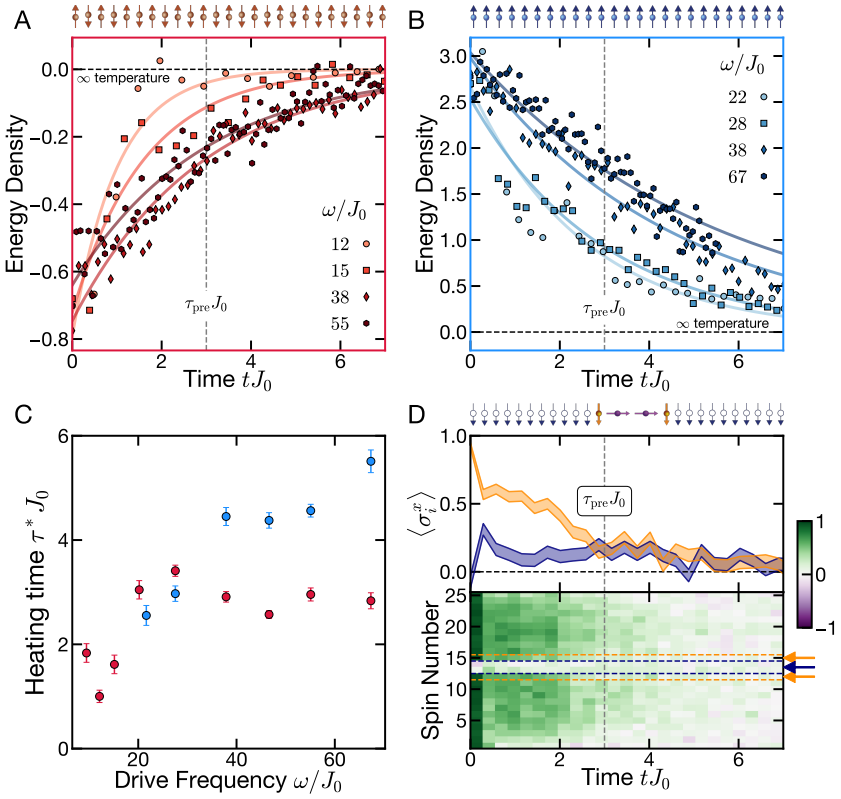

Figure 2: **Characterizing the prethermal regime. A, B.** The dynamics of the energy density for a low-energy Néel state (left) and a high-energy polarized state (right) highlights the frequency dependence of the heating rate. Statistical error bars are of similar size as the point markers. **C.** Heating time τ^* for the Néel (red) and polarized (blue) states, extracted via an exponential fit ($\sim e^{-t/\tau^*}$) to the energy density dynamics (solid curves in A and B). The presence of external noise leads to a saturation of τ^* at high frequencies. Error bars for the heating time correspond to fit errors. **D.** Characterization of the prethermal equilibration time, $\tau_{\rm pre}$, via the local $\hat{x}$-magnetization dynamics for even Floquet periods. Top: The middle two spins (purple), initially prepared along the $\hat{z}$ axis, rapidly align with their neighbors (orange) at time $\tau_{\rm pre}J_0 \approx 3$, signaling local equilibration to the prethermal state. The shaded bands represent the standard error of the mean. Bottom: $\hat{x}$-magnetization dynamics across the entire ion chain.

consequence of the periodic driving protocol (*30, 31*). In our experiment, this symmetry corresponds to a global spin flip, $G \approx U_1 \propto \prod_{i=1}^{N} \sigma_i^y$; indeed G is not a symmetry of the original evolution (Eq. 1) but it is present in H_{eff} (Eq. 2). When such emergent symmetry is present, the exact Floquet dynamics are approximately generated by evolving under H_{eff} for time T, followed by the action of G. This latter part suggests that the time-crystalline order is naturally captured by the system's magnetization dynamics; the action of G changes the sign of the order parameter $\langle \sigma_i^x \rangle$ every period. As a result, there are two possibilities for the prethermal dynamics, depending on the system's energy density (Fig. 1B). If the prethermal state corresponds to the symmetry-respecting paramagnet, the magnetization is zero and remains unchanged across a period. Conversely, if the prethermal state corresponds to the symmetry-breaking ferromagnet, the magnetization is nonzero and alternates every period. The resulting $2T$-periodic, sub-harmonic dynamics is the hallmark of a time crystal.

We investigate these two regimes by measuring the auto-correlation of the magnetization:

$$M(t) = \frac{1}{N} \sum_{i=1}^{N} \langle \sigma_i^x(t) \rangle \langle \sigma_i^x(0) \rangle. \tag{3}$$

Starting with a low-energy-density Néel state (Fig. 3A), we observe that $M(t)$ quickly decays to zero at τ_{pre}, in agreement with the expectation that the system equilibrates to the symmetry-unbroken, paramagnetic phase. This behavior is frequency-independent, in direct contrast to the Floquet dynamics of the energy density (Fig. 2A). This contrast highlights an essential point: although τ^* can be extended by increasing the driving frequency, no order survives beyond τ_{pre} when the system is in the trivial Floquet phase.

The Floquet dynamics starting from the polarized state are markedly distinct (Fig. 3B). First, $M(t)$ exhibits period doubling, with $M > 0$ for even periods and $M < 0$ for odd periods. Second, the decay of this period-doubling behavior is directly controlled by the frequency of the drive. Third, the lifetime of the time-crystalline order mirrors the dynamics of the energy

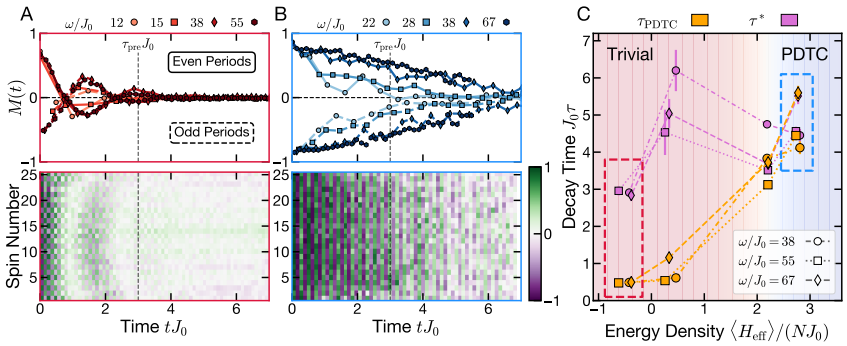

Figure 3: **Characterizing the PDTC phase. A, B.** Upper plots: Magnetization dynamics, $M(t)$, for the Néel state (left) and the polarized state (right). For the Néel state, $M(t)$ quickly decays to zero at time $\tau_{\rm pre}$ (dashed vertical line), independent of the drive frequency. For the polarized state, the sub-harmonic response ($2T$-periodicity) persists well-beyond $\tau_{\rm pre}$ and its lifetime is extended upon increasing the drive frequency. The lifetime of the prethermal time-crystalline order $\tau_{\rm PDTC}$ is obtained by fitting the magnetization dynamics to an exponential decay (*35*). Statistical error bars are of similar size as the point markers. Lower plots: $\hat{x}$-magnetization dynamics across the entire ion chain at $\omega/J_0 = 38$. **C.** Heating (τ^*) and magnetization decay ($\tau_{\rm PDTC}$) times for four different initial states at varying energy densities (*35*). At low energy densities, $\tau_{\rm PDTC}$ (orange) are significantly shorter than τ^* (magenta) and independent of frequency, highlighting the trivial Floquet phase. At high energies, $\tau_{\rm PDTC}$ is similar to τ^*, highlighting the long-lived, frequency-controlled nature of the PDTC behavior. The location of the observed crossover in energy density is in agreement with an independent quantum Monte Carlo calculation (red and blue shaded regions) (*35*). Error bars for the decay time correspond to fit errors, while error bars for the energy density correspond to statistical errors.

density shown in Fig. 2B, demonstrating that Floquet heating ultimately melts the PDTC at late times.

By considering two additional initial states, we explore the stability of the PDTC phase as a function of energy density. Fig. 3C depicts both the heating time as well as the lifetime of the time-crystalline order. Near the bottom of the spectrum, where no symmetry-breaking phase exists, the decay of the magnetization is frequency-independent and significantly faster than the heating timescale. By contrast, near the top of the spectrum, where a symmetry-breaking ferromagnetic phase exists, the two timescales are consistent with one another and thus Floquet heating limits the PDTC lifetime. Our results are consistent with a phase boundary occurring at energy density $\langle H_{\text{eff}} \rangle / (N J_0) \approx 2$, in agreement with independent numerical calculations via quantum Monte Carlo (*35*).

In this work, we report the experimental observation of robust prethermal time-crystalline behavior that persists beyond any early-time transient dynamics. Our results highlight the potential of periodic driving, in general, and prethermalization, in particular, as a framework for realizing and studying out-of-equilibrium phenomena. Even in the presence of noise, we find that the prethermal dynamics remain stable, suggesting that an external bath at sufficiently low temperature can stabilize the prethermal dynamics for infinitely long times (*30*). This stands in contrast to localization-based approaches for stabilizing Floquet phases, in which the presence of an external bath tends to destabilize the dynamics. Our work points to a number of future directions: (i) exploring generalizations of Floquet prethermalization to a quasi-periodic drive (*36*), (ii) stabilizing Floquet topological phases (*37, 38*), and (iii) leveraging non-equilibrium many-body dynamics for enhanced metrology (*39*).

References

1. L. D. Landau, E. M. Lifshitz, *Mechanics, Third Edition: Volume 1 (Course of Theoretical Physics)* (Butterworth-Heinemann, 1976), third edn.

2. P. Mansfield, *Journal of Physics C: Solid State Physics* **4**, 1444–1452 (1971).

3. L. M. K. Vandersypen, I. L. Chuang, *Reviews of Modern Physics* **76**, 1037–1069 (2005).

4. H. Zhou, *et al.*, *Physical Review X* **10**, 031003 (2020).

5. T. Oka, S. Kitamura, *Annual Review of Condensed Matter Physics* **10**, 387–408 (2019).

6. A. C. Potter, T. Morimoto, A. Vishwanath, *Physical Review X* **6**, 041001 (2016).

7. F. Nathan, D. Abanin, E. Berg, N. H. Lindner, M. S. Rudner, *Physical Review B* **99**, 195133 (2019).

8. D. V. Else, B. Bauer, C. Nayak, *Physical Review Letters* **117**, 090402 (2016).

9. N. Yao, A. Potter, I.-D. Potirniche, A. Vishwanath, *Physical Review Letters* **118**, 030401 (2017).

10. S. Choi, *et al.*, *Nature* **543**, 221–225 (2017).

11. J. Zhang, *et al.*, *Nature* **543**, 217–220 (2017).

12. J. Rovny, R. L. Blum, S. E. Barrett, *Physical Review Letters* **120**, 180603 (2018).

13. J. Smits, L. Liao, H. T. C. Stoof, P. van der Straten, *Physical Review Letters* **121**, 185301 (2018).

14. Z. Gong, R. Hamazaki, M. Ueda, *Physical Review Letters* **120**, 040404 (2018).

15. N. Y. Yao, C. Nayak, L. Balents, M. P. Zaletel, *Nature Physics* **16**, 438 (2020).

16. L. D'Alessio, M. Rigol, *Physical Review X* **4**, 041048 (2014).

17. D. A. Abanin, E. Altman, I. Bloch, M. Serbyn, *Reviews of Modern Physics* **91**, 021001 (2019).

18. N. Yao, *et al.*, *Physical Review Letters* **113**, 243002 (2014).

19. W. De Roeck, F. Huveneers, *Physical Review B* **95**, 155129 (2017).

20. S. Autti, V. Eltsov, G. Volovik, *Physical review letters* **120**, 215301 (2018).

21. K. Giergiel, *et al.*, *New Journal of Physics* **22**, 085004 (2020).

22. S. Autti, *et al.*, *Nature Materials* **20**, 171 (2021).

23. D. V. Else, C. Monroe, C. Nayak, N. Y. Yao, *Annual Review of Condensed Matter Physics* **11** (2020).

24. C. Monroe, *et al.*, *arXiv:1912.07845* (2019).

25. T. Kuwahara, T. Mori, K. Saito, *Annals of Physics* **367**, 96–124 (2016).

26. D. A. Abanin, W. De Roeck, W. W. Ho, F. Huveneers, *Physical Review B* **95**, 014112 (2017).

27. F. Machado, G. D. Kahanamoku-Meyer, D. V. Else, C. Nayak, N. Y. Yao, *Physical Review Research* **1**, 033202 (2019).

28. A. Rubio-Abadal, *et al.*, *Physical Review X* **10**, 021044 (2020).

29. P. Peng, C. Yin, X. Huang, C. Ramanathan, P. Cappellaro, *Nature Physics* p. 1–4 (2021).

30. D. V. Else, B. Bauer, C. Nayak, *Physical Review X* **7**, 011026 (2017).

31. F. Machado, D. V. Else, G. D. Kahanamoku-Meyer, C. Nayak, N. Y. Yao, *Physical Review X* **10**, 011043 (2020).

32. V. Khemani, R. Moessner, S. L. Sondhi, *arXiv:1910.10745* (2019).

33. L. Landau, *Zh. Eksp. Teor. Fiz.* **7**, 19 (1937).

34. K. Mølmer, A. Sørensen, *Physical Review Letters* **82** (1999).

35. See Supplementary material.

36. D. V. Else, W. W. Ho, P. T. Dumitrescu, *Physical Review X* **10**, 021032 (2020).

37. I.-D. Potirniche, A. C. Potter, M. Schleier-Smith, A. Vishwanath, N. Y. Yao, *Physical Review Letters* **119**, 123601 (2017).

38. D. V. Else, P. Fendley, J. Kemp, C. Nayak, *Physical Review X* **7**, 041062 (2017).

39. S. Choi, N. Y. Yao, M. D. Lukin, *arXiv:1801.00042* (2017).

40. K. Kim, *et al.*, *Physical Review Letters* **103** (2009).

41. D. James, *Applied Physics B: Lasers and Optics* **66** (1998).

42. S. Olmschenk, *et al.*, *Physical Review A* **76** (2007).

43. K. R. Brown, A. W. Harrow, I. L. Chuang, *Physical Review A* **70** (2004).

44. A. C. Lee, *et al.*, *Physical Review A* **94** (2016).

45. D. Wineland, *et al.*, *Journal of Research of the National Institute of Standards and Technology* **103** (1998).

46. C.-C. J. Wang, J. K. Freericks, *Physical Review A* **86** (2012).

47. L. Egan, *et al.* (2020).

Acknowledgments

We acknowledge fruitful discussions with C. Laumann, W. L. Tan, A. Vishwanath, D. Weld, and J. Zhang. **Funding:** This work is supported by the DARPA Driven and Non-equilibrium Quantum Systems (DRINQS) Program D18AC00033, NSF Practical Fully-Connected Quantum Computer Program PHY-1818914, the DOE Basic Energy Sciences: Materials and Chemical Sciences for Quantum Information Science program DE-SC0019449, the DOE High Energy Physics: Quantum Information Science Enabled Discovery Programs DE-0001893, the AFOSR MURI on Dissipation Engineering in Open Quantum Systems FA9550-19-1-0399, the David and Lucile Packard foundation, the W. M. Keck foundation, and the EPiQS Initiative of the Gordon and Betty Moore Foundation GBMF4303. **Author contributions:** A.K., W.M., P.B., K.S.C., L.F., P.W.H., G.P., and C.M. designed and performed experimental research, F.M., D.V.E., C.N., and N.Y.Y. analyzed the data theoretically, and all authors wrote the paper. **Competing interests:** C.M. is the co-founder and Chief Scientist at IonQ, Inc. **Data availability:** All data needed to evaluate the conclusions in the paper are present in the paper or the Supplementary Materials.

Supplementary materials

Supplementary text

Supporting numerical evidence

Figs. S1 to S6

References (*40–47*)

Supplementary materials

The trapped-ion quantum simulator

The quantum simulator used in this work is based on a chain of $^{171}\mathrm{Yb}^{+}$ ions trapped in a 3-layer Paul trap at room temperature (*40*). The ions are confined in all three directions by a combination of static and oscillating electric fields. The interplay of the repulsive Coulomb force and the trapping potential arrange the ions in a linear configuration. The transverse center-of-mass (COM) motional mode frequency along the $\hat{x}$ axis is $f_{\mathrm{COM}} = 4.67$ MHz and the axial COM frequency is $f_z = 0.34$ MHz. The axial trapping strength is set such that 25 ions settle in a linear configuration with inter-ion spacings varying from ~ 2 μm (chain center) to ~ 3.5 μm (chain edges) (*41*).

Spin and motional state preparation

Between experiments, the ions are Doppler cooled by a 369.5 nm laser red-detuned from the $^2S_{1/2}$ to $^2P_{1/2}$ transition by 10 MHz, one-half of the transition linewidth. This laser projects onto all three principle axes of the trap, ensuring that the ions are cooled along all directions. To begin an experiment, the ions are initialized in the low-energy hyperfine qubit state $|{\downarrow}\rangle \equiv {}^2S_{1/2}|F = 0, m_F = 0\rangle$ by an incoherent optical pumping process (*42*). Optical pumping requires approximately 20 μs and initializes all ions to $|{\downarrow}\rangle$ with at least 99 % fidelity. At this point the individual spin states of the ions are well-known, while the shared motional state is a thermal distribution with $\bar{n} \leq 3$ average motional quanta in the transverse $\hat{x}$ axis modes. Resolved sideband cooling on multiple motional modes brings the ions near their motional ground state ($\bar{n} \leq 0.1$ average motional quanta).

With the ions cooled and their spin states initialized, we prepare the spins in product states along the $\hat{x}$ axis of the Bloch sphere with a combination of global rotations and individual σ^z rotations. Global rotations are driven with a pair of Raman laser beams, intersecting at a 90°

angle. These lasers produce a beatnote that drives oscillations between the qubit states with Rabi frequency Ω when tuned on resonance with the ions' S-manifold hyperfine splitting. The phase of this beatnote determines the Bloch sphere axis about which the spins are rotated.

The BB1 pulse sequence

Each Raman beam has a Gaussian intensity profile with waists of 10 μm by 130 μm at the ion plane. A 25-ion chain has a length of about 60 μm. Each ion samples a slightly different intensity from the Raman lasers, resulting in different rates of rotation across the chain. To minimize rotation errors caused by this inhomogeneity during the U_1 unitary, we employ BB1 dynamical decoupling sequences (*43*) to ensure that all spins along the chain are rotated by the same amount.

A traditional $\hat{y}$ rotation unitary has the form $\hat{U}_\theta^y = e^{-i\theta\sigma_i^y/2}$, where θ is the desired angle of rotation about the $\hat{y}$ axis. The angle $\theta \equiv \Omega_i t$, where Ω_i is the Rabi frequency experienced by spin i, is sensitive to the spacially-inhomogeneous intensity profiles of the Raman lasers. We instead apply the following BB1 unitary, consisting of 4 sub-rotations:

$$\hat{U}_{\theta,\mathrm{BB1}}^y = e^{-i\frac{\pi}{2}\sigma_i^\phi} e^{-i\pi\sigma_i^{3\phi}} e^{-i\frac{\pi}{2}\sigma_i^\phi} e^{-i\frac{\theta}{2}\sigma_i^y}. \tag{4}$$

The phase ϕ depends on the desired rotation angle θ:

$$\phi = \arccos\left(\frac{\theta}{4\pi}\right). \tag{5}$$

While a π-rotation using this sequence takes five times longer than a traditional rotation pulse, it reduces rotation errors significantly and prevents dephasing across the chain. This allows us to apply hundreds of π-pulses with negligible loss of contrast—a requirement for the time-crystal experimental sequences presented in this manuscript.

Arbitrary product state preparation

An individual addressing beam focused to a waist of 500 nm generates rotations on each spin with relatively low crosstalk. A high-bandwidth acousto-optical deflector (AOD) steers the beam, and the AOD's rf drive frequency maps the beam to a location along the ion chain. This beam applies a fourth-order AC Stark shift to the hyperfine qubit splitting (*44*), creating an effective σ_i^z rotation on a single spin i. This rotation is mapped to a rotation about any axis using the appropriate global analysis $\pi/2$ rotations, allowing for preparation of product states with arbitrary spin flips such as the antiferromagnetic Néel state.

Qubit readout

At the end of an evolution, we measure the magnetization of each spin using state-dependent fluorescence. A 369.5 nm laser resonant with the $^2S_{1/2}|F=1\rangle \leftrightarrow {}^2P_{1/2}|F=0\rangle$ transition (linewidth $\gamma/2\pi \approx 19.6$ MHz) causes each ion to scatter photons if the qubit is projected to the $|\uparrow\rangle$ state. Ions projected to the $|\downarrow\rangle$ qubit state scatter a negligible number of photons because the laser is detuned from resonance by the $^2S_{1/2}$ hyperfine splitting. By applying global $\pi/2$-rotations, we rotate the x and y bases into the z basis. This allows us to measure all individual magnetizations and many-body correlators along any single axis. In the experiments reported in this work, we repeat the experimental sequence and the measurement for 50-600 times to reduce quantum projection noise.

For each measurement, a finite-conjugate $NA = 0.4$ objective lens system (total magnification of $70\times$) collects scattered 369.5 nm photons and images them onto an Andor iXon Ultra 897 EMCCD camera. Before taking data, high-contrast calibration images of the ion chain, illuminated by Doppler cooling light, are used to identify a region of interest (ROI) on the camera sensor for each ion. During data collection, fluorescence is integrated for 400 μs, after which a pre-calibrated binary threshold is applied to discriminate the qubit state of each ion

with approximately 98 % accuracy per ion.

The dominant error sources for the qubit readout, ordered by decreasing significance, are: mixing of qubit states caused by off-resonant coupling during the 400 μs camera exposure window, crosstalk between ion ROIs due to small inter-ion spacings near the center of the chain, electronic camera noise, and laser power fluctuations. No state preparation and measurement (SPAM) correction has been applied to data presented in this work.

Simulating the transverse field Ising Hamiltonian

We generate the effective spin-spin interaction Hamiltonian by applying spin-dependent dipole forces with the pair of 355 nm Raman beams mentioned earlier. These beams produce a beatnote with wavevector $\Delta\vec{k}$ aligned along a principle axis of the trap. The frequencies of these beams are controlled with acousto-optical modulators (AOMs) to generate a pair of beatnote frequencies detuned by $-\mu$ (red beatnote) and $+\mu$ (blue beatnote) from the resonant qubit transition frequency. For $\mu - f_{COM} \gg \eta\Omega$ (η is the Lamb-Dicke parameter (*45*)) and $\eta \ll 1$, the experiment operates in the far-detuned Mølmer-Sørensen (MS) regime (*34, 40*). Here, excited motional states are adiabatically eliminated and the laser-ion interaction takes the form of a spin-spin, effective long-range interacting Ising Hamiltonian

$$H = \sum_{i<j}^{N} J_{ij}\sigma_i^x\sigma_j^x. \tag{6}$$

The $N \times N$ matrix J_{ij} describes couplings between spins i and j (Fig. S1):

$$J_{ij} = \Omega^2 f_R \sum_{m=1}^{N} \frac{b_{im}b_{jm}}{\mu^2 - f_m^2} \tag{7}$$

where $f_R = \Delta k^2/(2M)$ is the recoil frequency, f_m is the frequency of the m-th motional mode, b_{im} is the eigenvector matrix element of the i-th ion's participation in the m-th motional mode

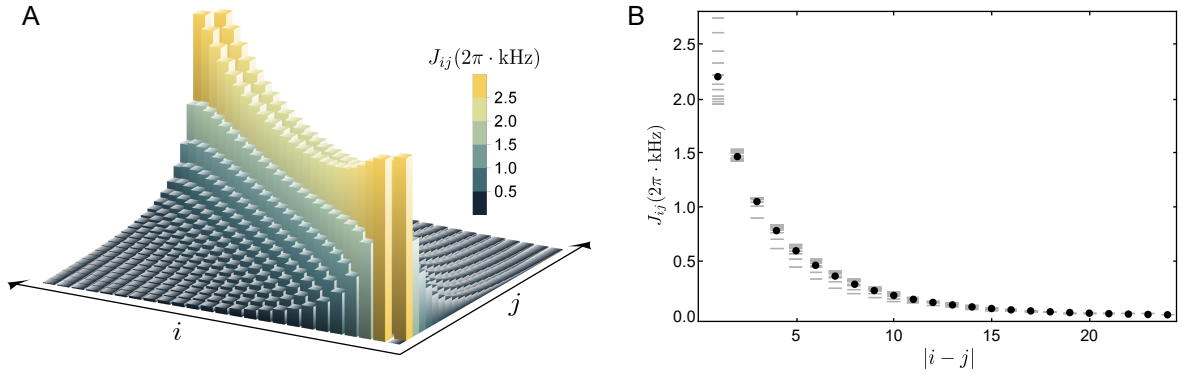

Figure S1: **The interaction matrix J_{ij}. A.** The position of each column represents a pair of spins $\{i, j\}$, while its color-coded height the strength of their coupling. **B.** To illustrate how the interaction strength scales with distance between i and j, we average the elements of the diagonals of J (circular markers), e.g. the $|i-j|=2$ corresponds to $\langle\{J_{13}, J_{24}, J_{35}, J_{46}, \ldots\}\rangle$. The line markers illustrate all the individual couplings for that value of $|i-j|$.

($\sum_i |b_{im}|^2 = \sum_m |b_{im}|^2 = 1$), and M is the mass of a single ion. Using $\eta_m = \sqrt{f_R/f_m}$, we get

$$J_{ij} \approx \frac{\Omega^2}{2} \sum_{m=1}^{N} \frac{b_{im} b_{jm} \eta_m^2}{\delta} \tag{8}$$

In the reported experiments, the average nearest-neighbor interaction $J_0/(2\pi) = 0.33 \pm 0.02$ kHz.

We add transverse fields to Eq. 6 in two ways. To create an effective transverse field B_z along the $\hat{z}$ direction, we apply a global offset of $2B_z$ to the two Raman beatnote frequencies, imposing a rotating frame shift between the qubit and the beatnotes to generate an effective field with strength B_z. A third Raman beatnote, resonant with the qubit transition and applied simultaneously with the Mølmer-Sørensen red and blue beatnotes, creates additional transverse fields along the $\hat{x}$ or $\hat{y}$ directions depending on the beatnote phase. Altogether, the long-range, transverse-field Ising Hamiltonian takes the form

$$H = \sum_{i<j}^{N} J_{ij} \sigma_i^x \sigma_j^x + B_y \sum_i^N \sigma_i^y + B_z \sum_i^N \sigma_i^z. \tag{9}$$

Tukey window pulse shaping

All Raman laser operations and individual-addressing operations are implemented via amplitude modulation of the rf that drives various AOMs and AODs. An arbitrary-wavefrom generator (AWG) outputs this amplitude-modulated rf signal to switch lasers and beatnotes on and off according to the experimental sequence. If the control rf is modulated with square pulses, the sharp edges (limited by the rise/fall time of the AOM/D) cause significant spectral broadening of the signal in the Fourier domain. This effect is more pronounced for shorter pulses, such as the Raman pulses used to generate the unitary U_2. This spectral broadening can be on the order of MHz, and causes undesirable driving of qubit motional and spin transitions.

We suppress spectral broadening by applying Tukey window pulse shaping, where the first and last 10 μs of the pulse are multiplied respectively by a rising and falling sinusoidal envelope. We account for the resulting reduction in the magnitude of each term of the Hamiltonian by scaling it down by an appropriate factor, which varies with the total duration of that pulse. Longer pulses need to be scaled down less, since the ramp time is fixed.

Error sources

The dynamics observed in this work are the combination of ideal Hamiltonian evolution as in Eq. 1 and other terms of smaller magnitude that we refer to as "error sources". The combined effect of the latter, when measuring the chain magnetization, manifests as decoherence.

The most significant error source is fluctuating AC Stark shifts of the hyperfine qubit frequency. This fluctuation is mostly caused by power instability of the 355 nm laser light at the ions' location. Even though there is a power PI locking scheme in effect for the 355 nm light, the sampling point for the lock is at a more upstream location that the ions. As the beams propagate downstream from that point, active elements, acoustic noise, and air turbulence introduce extra power noise. At the ions location, the light's red and blue beatnotes ideally produce ex-

actly opposite AC Stark shifts of the qubit levels and cancel each other, in practice they are not always perfectly balanced. In this case, power fluctuations will make the sum of their Stark shifts fluctuate. This manifests as an effective fluctuating magnetic field term $B^{(AC)}(t)\sum_i \sigma_i^z$, common for all spins i and present in every stage of the experimental sequence. A fortunate side effect of the π-rotations of the drive is that they echo out part of this noise. However, the spectral portion of $B^{(AC)}(t)$ that is faster than $\omega/2$ is not echoed out and differs between different repetitions, manifesting as decoherence in the final averaged signal. In numerics presented in the next section, we model this noise based on experimental evidence and reasonable simplifications, and present numerical simulations that include it.

Imperfect qubit state readout also impacts the final fidelity of the simulation. During the finite readout window of 400μs, there is a small probability that a $|\downarrow\rangle$ state will be off-resonantly pumped, and read out as a $|\uparrow\rangle$ state, and vice versa. For the experiments presented in this work, the average readout error was 2.3% for each ion.

Another error source comes from a term combining the spin and the motional part of the qubit wavefunction that acts in parallel with the effective Ising interaction in Eq. (6). This term represents entanglement between these two parts; when we measure the qubit spin, we effectively trace out the entangled motional state, resulting in a probabilistic mixed state. The probability for such an erroneous spin flip to occur is proportional to

$$\sum_{m=1}^{N}\left(\frac{\eta_m b_{im}\Omega}{\delta_m}\right)^2 \tag{10}$$

Therefore, by increasing this detuning, we minimize the undesired spin-motion entanglement, but we are also decreasing the strength of our spin-spin interaction term (see Supplement, Simulating the transverse field Ising Hamiltonian). We set the balance between these effects by keeping the sum in Eq. (10) less than 0.1 for two spins, which for the 25 spins results in approximately 0.7% flip probability per spin. This effect is somewhat amplified by the finite duration

of the Hamiltonian quenches in the second term of the Floquet drive, whose spectral decomposition has nonzero components in the motional frequencies. We considerably mitigate this effect by applying the Tukey window shaping to the relevant pulses (see Supplement, Tukey window pulse shaping), which reduces these undesired spectral terms.

Other error sources provide smaller contributions to the observed decoherence. For example, with a small probability, an ion can be off-resonantly excited during the Ising evolution to a P-manifold state, scatter a photon, and decay to a state outside the qubit computational manifold. The probability of a single such event happening in the total chain is zero at the beginning of the Ising evolution and monotonically increases to approximately 10% at the end. A different source of error comes from the combination of the MS scheme generating the $\sigma_i^x \sigma_j^x$ interactions and the transverse field B_y (*24*). Terms involving σ_i^x, acting on the spins, and the ladder operators a and $a^\dagger$, acting on the motional wavefunction, arise in this case. In the far-detuned MS regime, these terms are perturbatively small compared to the transverse field term (*46*). Moreover, the frequencies of the ion chain normal modes show small drifts tracing temperature fluctuations in apparatus pieces. This leads to correspondingly small fluctuations of the interaction matrix profile J_{ij}. Because of the small magnitude of these effects and the difficulty in characterizing them, we do not explicitly account for them in the numerical simulations of noise in the next section. However, their effect is compounded with the dominant noise sources explicitly accounted for.

Extraction of τ_{PDTC}

Owing to the time translation symmetry breaking associated with the PDTC, the correct order parameter is one that is sensitive to the difference of the system during even and odd periods of the evolution. To this end, we define the magnetization difference ΔM as the order parameter

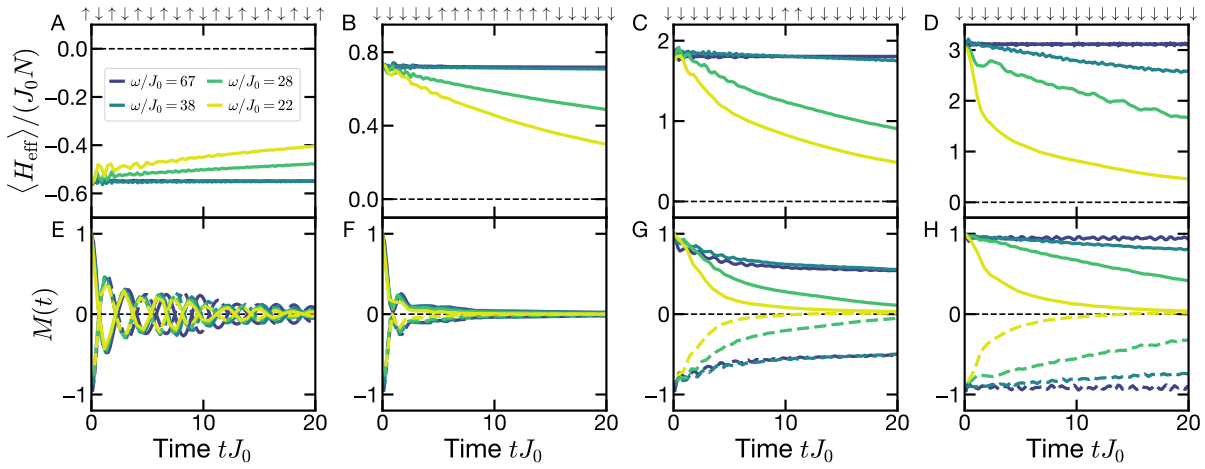

Figure S2: **PDTC dynamics in the absence of noise A-D.** Dynamics of the energy density $\langle H_{\rm eff}\rangle/NJ_0$ for different initial states with increasing energy density. The decay of the energy density to the late time infinite temperature value is exponentially sensitive to the frequency of the drive. **E-H.** Dynamics of the magnetization $M(t)$, for different initial states. Full[dashed] line corresponds to even[odd] periods. For low energy density, the magnetization is approximately frequency-independent, highlighting the trivial nature of the dynamics. For high energy density, the magnetization decay follows the decay of the energy density and exhibits a robust period doubling behavior—the two hallmarks of the PDTC.

we investigate:

$$\Delta M(t) = |M(t+T) - M(t)|. \tag{11}$$

$\tau_{\rm PDTC}$ is then extracted by fitting the dynamics of $\Delta M(t)$ to a simple exponential decay $\propto e^{-t/\tau_{\rm PDTC}}$.

Supporting numerical evidence

Dynamics in the absence and presence of noise

In this section, we present a numerical investigation of the dynamics simulated by the experimental platform, highlighting the physics of prethermalization and the PDTC. We first focus on the noiseless case, where we observe the expected exponential frequency dependence of τ^* on the drive frequency ω, and then turn to studying the effect of noise on the observed dynamics.

We consider an $N = 19$ spin chain with interactions given by the experimentally determined interaction matrix for 25 spins, truncated to the middle 19 spins. We perform the exact time evolution of the full quantum system using Krylov subspace methods, simulating the entire experimental protocol (which includes the Tukey window pulse shaping).

For all states considered (Fig. S2), we observe the same effect of the frequency on the heating timescale τ^*—the larger the frequency, the slower the energy approach to its infinite temperature value. By contrast, the dynamics of the magnetization can be starkly different. For the states at low enough energy density, where H_{eff} does not exhibit a spontaneous symmetry-breaking phase, the dynamics of $M(t)$ are mostly frequency-independent, and much faster than the heating. For states near the top of the spectrum, where a spontaneous symmetry-breaking phase exists, the dynamics of the magnetization exhibit robust period doubling whose decay matches that of the energy density—this is PDTC behavior. We summarize the timescales observed in Fig. S3, where the frequency dependence of τ^* occurs across all initial states, while the frequency dependence of τ_{TC} only occurs at the top of the spectrum.

We now turn to simulating the effect of noise in the observed dynamics. As mentioned in Error sources, the most significant noise arises from laser power fluctuations. We parameterize these fluctuations at the ions' location with the random variable $\epsilon(t)$, characterized by a flat spectrum and standard deviation σ over a given duration (we have found that results are independent of the upper frequency cutoff as long as it is much larger than the drive frequency) . We model this effect in the dynamics by adding a time dependence on the different parameters, B_y, B_z and J_{ij}:

$$B_y(t) = B_y^{\text{static}} \times [1 + \epsilon(t)] \tag{12}$$

$$B_z(t) = B_z^{\text{static}} + \epsilon(t) \times 2\pi \times 8\text{kHz} \tag{13}$$

$$J_{ij}(t) = J_{ij}^{\text{static}} \times [1 + 2\epsilon(t)] \tag{14}$$

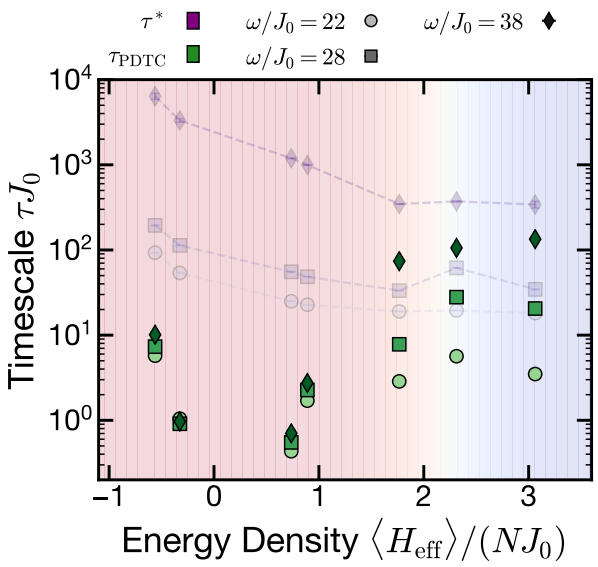

Figure S3: **PDTC timescales in absence of noise**. Summary of the decay time scales of energy density (τ^*) and magnetization ($\tau_{\rm PDTC}$). In the region where $H_{\rm eff}$ exhibits a spontaneous symmetry broken phase (blue shading), $\tau_{\rm PDTC}$ follows the frequency dependence of τ^*. By contrast, outside this region, the $\tau_{\rm PDTC}$ is much smaller than τ^* and is mostly frequency-independent.

The dependence of each term on $\epsilon(t)$ is determined by the way that the laser power relates to that term, eg. the $B_y(t)$ field depends linearly on the 2-photon Rabi frequency Ω, which is proportional to laser power. In Fig. S4, we highlight the effect of noise in two states at opposite sides of the spectrum and also considered in the main text: the polarized state and the Néel state. The effect on either is qualitatively similar: noise reduces the frequency control of the Floquet heating leading to a plateau in the achievable τ^*, in agreement with the experimental observation (we highlight this feature in Fig. S5). It is important to emphasize two points. First, while for large frequency the noise dominates the heating towards the infinite temperature state, the frequency still provides a control of the Floquet heating highlighting the importance of of the drive. Second, the dynamics of the magnetization is distinct in the trivial and the PDTC regimes. In the former, the magnetization quickly decays before the heating time scale while in the latter, the magnetization decay follows the energy density decay.

We note that the approximate character of the noise model leads to fitted noise values σ higher than typically quoted single- or two-qubit gate errors in quantum computing devices with trapped ions (*47*). This difference is related to the gate-based nature of the evolution which leads to a more efficient mitigation of noise using stronger interaction strengths (than our nearest neighbor coupling J_0) and with the aid of schemes (such as SK1 composite pulses (*47*)) to mitigate the effect of noise. The continuous evolution under the Ising Hamiltonian cannot benefit from such schemes.

Computing the crossover between trivial and PDTC behavior

Since the PDTC behavior is dependent on a spontaneous symmetry-broken phase in H_{eff}, we can calculate the boundary between trivial and PDTC behavior by mapping the location of the transition (which for finite system size will emerge as a crossover). In particular, owing to the antiferromagnetic interactions $J_{ij} > 0$, we are interested in the properties of the top of the spectrum, where the system orders ferromagnetically. To this end, we perform a quantum Monte Carlo simulation of the Hamiltonian $-H_{\text{eff}}$ in an $N = 25$ spin chain (Eq. 2), which maps the calculation to the more common problem of finding the low-temperature phase boundary of the para-to-ferromagnetic phase. In Fig. S6 we present the results in terms of the original energy density. By the system extending into the imaginary time dimension, we can perform the calculation at finite temperature $1/\beta$ and extract the crossover temperature and then map it to the relevant crossover energy density. In particular, we identify the location of the crossover by the location of the peak in the heat capacity of the system which we fit to a Lorentzian peak, while the width is taken to be the quarter-width half-max of the peak. The crossover location is then given by: $\epsilon/J_0 = 2.18 \pm 0.60$.

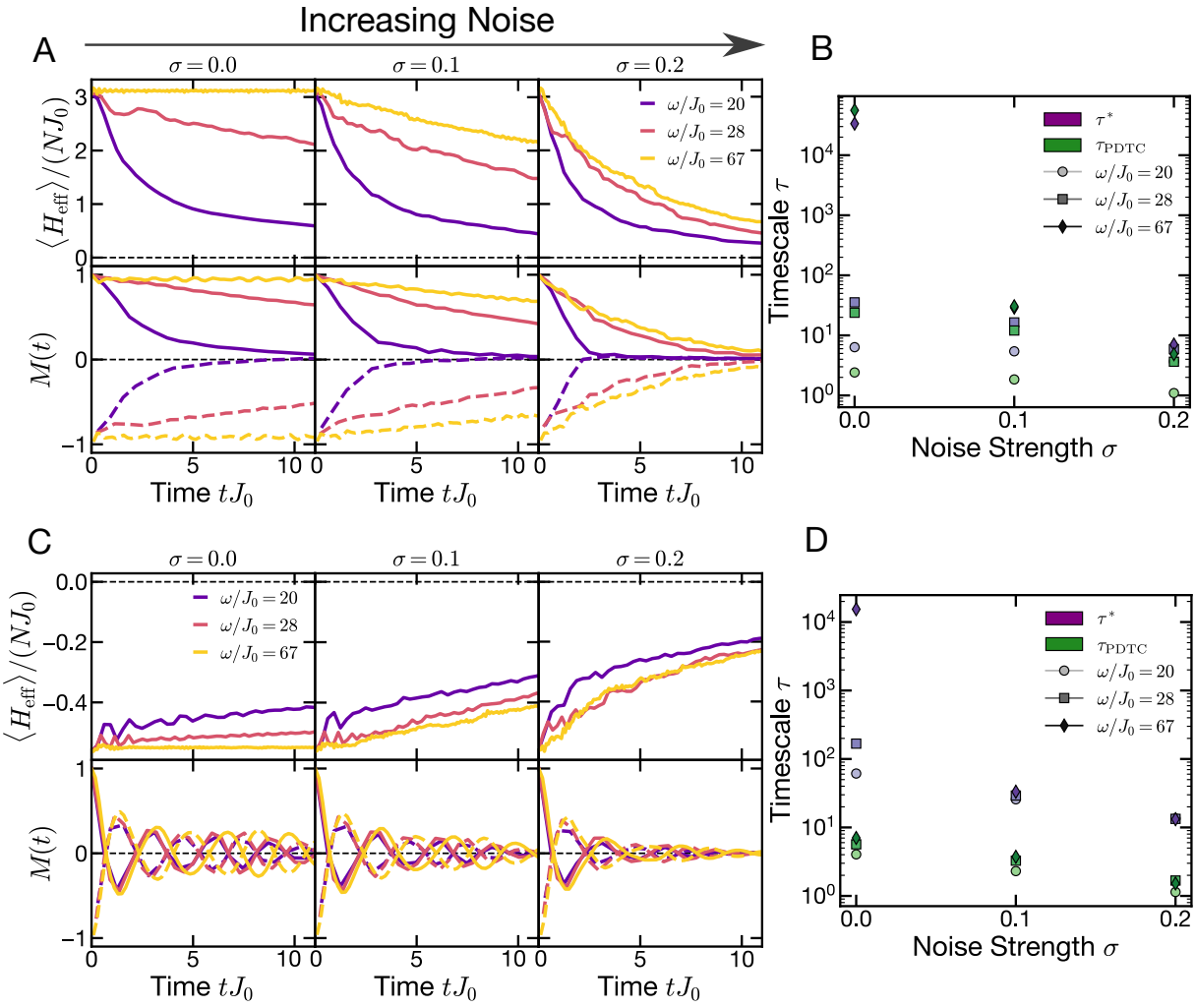

Figure S4: **Impact of noise on the PDTC and trivial Floquet dynamics** Heating dynamics of the polarized state (**A-B**) and the Néel state (**C-D**) for different strength of the noise σ. The presence of noise hastens heating to the infinite temperature state, setting an upper bound on the time scales. Nevertheless, the trivial dynamics can be distinguished from the PDTC behavior. In the former, the magnetization decay remains frequency independent and much faster than the energy decay. In the latter, the magnetization decay has a similar frequency dependence to the energy density decay.

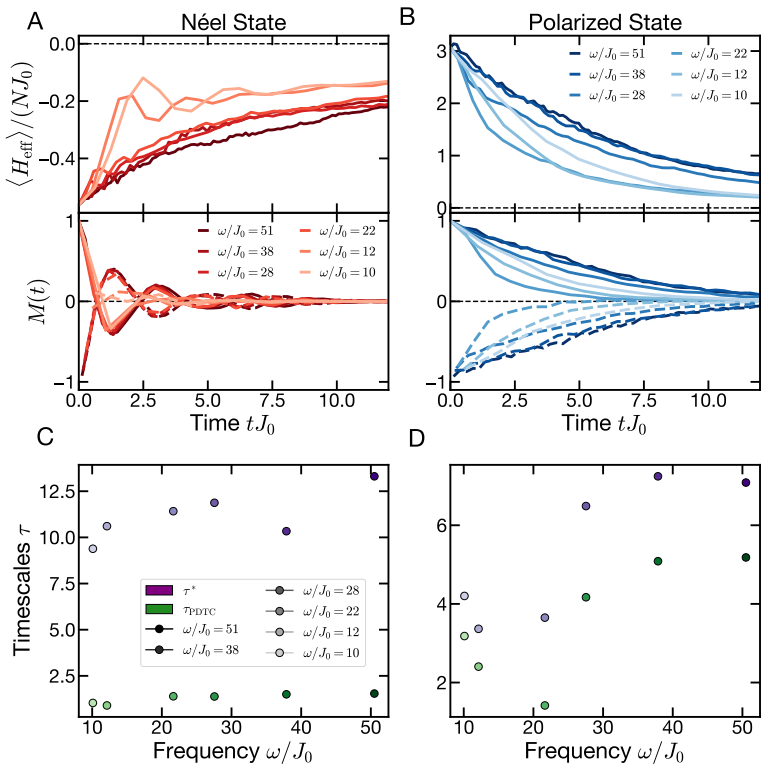

Figure S5: **Frequency dependence of the heating τ^* and time-crystalline $\tau_{\rm PDTC}$ timescales for fixed strength of the noise. A-B.** Energy (top) and magnetization (bottom) dynamics for the Néel and the polarized initial state, in the presence of noise with moderate strengths $\sigma = 0.1$. **C-D.** Upon increasing the frequency of the drive, we observe an increase in the heating time scale τ^* for both initial states, up until very high-frequencies where heating becomes dominated by the fluctuating noise. Crucially, the dynamics of the time-crystalline order is very different. For the Néel state, the time-crystalline order parameter decays quickly and is frequency independent—the system is in a trivial Floquet phase. For the polarized state, the increased heating time is mirrored by a increase of lifetime of the time-crystalline order parameter—the system is in the PDTC Floquet phase.

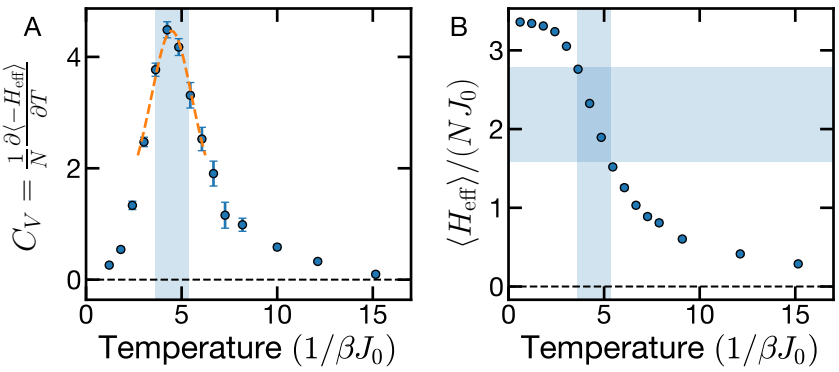

Figure S6: **Calculation of the para-to-ferromagnetic crossover region in $H_{\rm eff}$.** Quantum Monte Carlo calculation for the $N = 25$ spin chain considered in the experiment. **A.** We can locate the location and width of the crossover by characterizing the peak in the heat capacity C_V. **B.** Armed with the crossover temperature, we can directly map it into the crossover energy density which yields: $H_{\rm eff}/(NJ_0) = 2.18 \pm 0.60$.